Article

Gold-Hydrogel Nanocomposites for High-Resolution Laser-Based 3D Printing of Scaffolds with SERS-Sensing Properties

Isabel Ventisette,[#] Francesco Mattii,[#] Caterina Dallari, Claudia Capitini, Martino Calamai, Beatrice Muzzi, Francesco S. Pavone, Federico Carpi, and Caterina Credi*

Read Online

ACCESS | Metrics & More | Article Recommendations | Supporting Information

ABSTRACT: Although visible light-based stereolithography (SLA) represents an affordable technology for the rapid prototyping of 3D scaffolds for in vitro support of cells, its potential could be limited by the lack of functional photocurable biomaterials that can be SLA-structured at micrometric resolution. Even if innovative photocomposites showing biomimetic, bioactive, or biosensing properties have been engineered by loading inorganic particles into photopolymer matrices, main examples rely on UV-assisted extrusion-based low-resolution processes. Here, SLA-printable composites were obtained by mixing a polyethylene glycol diacrylate (PEGDA) hydrogel with multibranched gold nanoparticles (NPs). NPs were engineered to copolymerize with the PEGDA matrix by implementing a functionalization protocol involving covalent grafting of allylamine molecules that have C=C pendant moieties. The formulations of gold nanocomposites were tailored to achieve high-resolution fast prototyping of composite scaffolds via visible light-based SLA. Furthermore, it was demonstrated that, after mixing with a polymer and after laser structuring, gold NPs still retained their unique plasmonic properties and could be exploited for optical detection of analytes through surface-enhanced Raman spectroscopy (SERS). As a proof of concept, SERS-sensing performances of 3D printed plasmonic scaffolds were successfully demonstrated with a Raman probe molecule (e.g., 4-mercaptobenzoic acid) from the perspective of future extensions to real-time sensing of cell-specific markers released within cultures. Finally, biocompatibility tests preliminarily demonstrated that embedded NPs also played a key role by inducing physiological cell-cytoskeleton rearrangements, further confirming the potentialities of such hybrid nanocomposites as groundbreaking materials in laser-based bioprinting.

KEYWORDS: stereolithography, PEGDA, nanocomposites, gold nanoparticles (AuNPs), surface enhanced Raman spectroscopy, allylamine-conjugated NPs, optical sensing
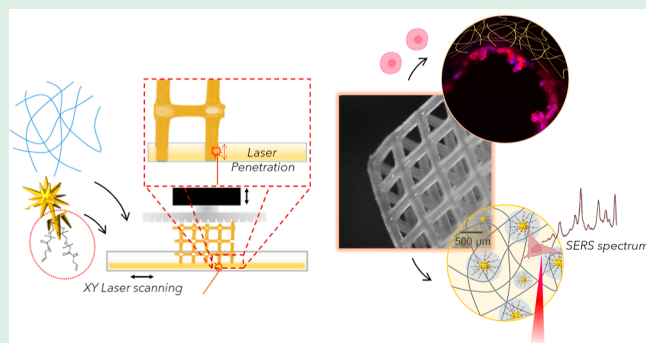
INTRODUCTION

To date, in vitro three-dimensional (3D) synthetic structures are widely recognized as a concrete alternative to traditional planar cell cultures due to their unique capability to simultaneously mimic the structural and functional *in vivo* microenvironment for cell proliferation and differentiation.[1],[2] To this end, innovative materials with biomimetic, bioactive, and biosensing properties have been engineered to be microstructured with 3D printing processes. Indeed, 3D printing techniques are well-established methods for the rapid prototyping of complex geometries resembling cell spatial organization at the varied organ-level structures.[3−6] Among all, photopolymerization-based techniques, such as stereolithography (SLA) and two-photon polymerization (2PP), are exploited to manufacture scaffolds with tailored porosity, mimicking physiological extracellular matrices (ECMs).[7,8] Indeed, stem cell homing behavior has successfully been induced in 2PP structures with nanometric resolution
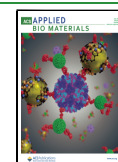
that is obtained by exploiting a nonlinear 2-photon absorption mechanism that confines the radiation. However, that method requires bulky and expensive equipment as well as long processing times.[9,10] Conversely, visible light-based SLA working in laser scanning configuration is an affordable technology that exploits a controlled spotlight to selectively polymerize a photocurable resin, enabling highly versatile low-cost fabrication of macro-structures with features down to the micrometric scale.[11] To push forward low-cost SLA technology, a plethora of novel 3D light-shapeable materials has been developed as scaffolding materials with improved biocompat-

ibility, active biofunctionality, as well as tunable stiffness.[4,7,8,12,13] Natural-derived hydrogels (e.g., hyaluronan, collagen, and gelatin) and synthetic-derived hydrogels (e.g., polyethylene glycol and derivatives, polycaprolactone) represent key candidates for the development of bioinks, recapitulating the ECM properties and functions.[14−17] From a 3D printing perspective, while their suitability has been widely demonstrated for extrusion-based 3D printing,[18,19] most examples reported for SLA using visible light remain limited to the fabrication of free-form microfluidics networks working as artificial vessels or in general to millimetric structures whose features are hundreds of microns.[20−23] In order to push the resolution down to the cell scale, in previous works on SLA printing, some of us adopted the strategy of doping the pristine photopolymers with organic and inorganic additives. These reduced the laser penetration depth in the photoresin by scattering or adsorbing photons and competing with the photoinitiator (PI).[7,12,13,24] As a step forward, the present work was focused on the development of novel functional SLA-printable composites obtained by mixing photocurable hydrogels with gold nanoparticles (NPs) representing one of the most widely studied nanosystems in the biomedical sector. In tissue engineering, it is reported that the integration of NPs into scaffolds could have an impact on cell proliferation and differentiation or could be used to trigger stimuli.[25−28] In biosensing applications, the plasmonic properties of NPs were exploited for the ultrasensitive detection of analytes via surface-enhanced Raman spectroscopy (SERS).[29],[30] Briefly, SERS exploits the surface-localized plasmons phenomena occurring upon NP-light interactions to amplify (up to 10^6) the Raman signal of analytes that are adsorbed onto NPs, thus providing the characteristic vibrational fingerprint of those adsorbed molecules with respect to the overall background. Consequently, the development of novel NP-loaded photopolymers opens interesting perspectives for the fast and low-cost printing of scaffolds at high resolution, guaranteeing improved cell adhesion and proliferation and showing intrinsic SERS-sensing capabilities. This additional functionality represents a potential tool for monitoring cell conditions through the detection of metabolites or other proteins secreted in the medium buffer. Despite these advantages, the examples reported on NP loading in 3D photocurable hydrogel-based matrices are limited to UV-assisted extrusion-based low-resolution processes.[31,32] Furthermore, they involved mixing the polymeric matrices with electrostatically stabilized NPs [e.g., citrate-capped NPs, hexadecyltrimethylammonium bromide (CTAB)-capped NPs] that lose their colloidal stability upon incubation with standard cells culture. Indeed, although the hydrogel porous network physically confining the NPs should improve their stability, the high ionic strength of the cell medium induces desorption of the capping agents from the gold surfaces, resulting in uncontrolled clustering of NPs that lose their SERS resonant properties.[33−35] To this end, we first reported a new functionalization protocol to decorate the NP surface with photoreactive pendant moieties, guaranteeing at once NPs' colloidal stability and covalent trapping via light-induced copolymerization with the hydrogel matrix. The two-step protocol was based on a standard ligand-exchange process to attach a PEG-derived bifunctional ligand, which contains thiols, for grafting to the gold surface, and a carboxyl end-chain group, for further conjugation of allylamine molecules with C=C pendant moieties through peptide bonds formation.[36],[37] To demonstrate their feasibility as a functional filler for SLA

nanocomposites, NPs decorated with C=C moieties were loaded in polyethylene glycol diacrylate (PEGDA), and their potential effect as photons scatterers or absorbers during the laser−photocomposite interaction was studied by quantifying the two SLA key parameters: the critical energy E_c, defined as the required energy dose to cross-link the resin, and the depth of penetration D_p, defined as the length of penetration of the laser within the resin.[38] Lower D_p and E_c values corresponded to thinner material slices (higher resolution), which could be deposited at faster polymerization rates (higher printing speed).[39,40] Following previous results,[12,13,24] an inert dye competing with the PI by absorbing photons was used as a coadditive to further confine the laser penetration. The best performing mixtures were subsequently successfully used for SLA printing of millimetric NP-loaded 3D structures, with geometrical features at resolutions down to tens of micrometers and with intrinsic SERS-based sensing capability. This was confirmed by acquiring SERS spectra of target molecules (e.g., 4-mercaptobenzoic acid Raman reporter) adsorbed on scaffold surfaces. Finally, the biocompatibility of 3D SERS-structures was also attested by performing cultures with HeLa human cells, whose proliferation and colonization of internal pores increased at increasing NPs loading. Furthermore, cell tests preliminarily demonstrated the capability of NPs to induce cell-cytoskeleton rearrangements resulting in cell morphology toward a physiological HeLa shape.

■ MATERIALS AND METHODS

Materials. All materials were purchased from Merck and used as received. The preparation of the photopolymer matrix required polyethylene glycol diacrylate (PEGDA—average molecular weight M_n = 700 Da), the photoinitiator (PI) 2,4,6-trimethylbenzoylphenyl phosphinate (TPO-L), and the brilliant yellow (BY) dye. NPs synthesis and functionalization required gold(III) chloride trihydrate (HAuCl$_4$·3H$_2$O), trisodium citrate dihydrate (C$_6$H$_5$O$_7$Na$_3$·2H$_2$O), L-(+)-ascorbic acid (AA), silver nitrate (AgNO$_3$), hydrochloric acid (HCl), nitric acid (HNO$_3$—70%), poly(ethylene glycol) 2-mercaptoethyl acetic acid (SH-PEG-COOH, M_n 7500 Da), N-[3-(dimethylamino)propyl]-N-ethylcarbodiimide hydrochloride (EDC), N-hydroxysuccinimide (NHS), and allylamine (AlAm). Milli-Q water was used in all of the experiments. All glassware used for NP synthesis were washed with aqua regia, rinsed several times with water, and dried before use. HeLa cells were obtained from ATCC (Manassas, VA, USA). Dulbecco's Modified Eagle's Medium (DMEM), glutamine, fetal bovine serum (FBS), penicillin/streptomycin solution (P/S), Leibovitz's L-15, and wheat germ agglutinin (WGA)-594 were purchased from Thermo Fisher Scientific (Waltham, MA, USA). Phosphate buffer saline (PBS) was purchased from Merck.

Synthesis and Functionalization of NPs. The gold NPs were synthesized following the seeded-growth process described by Yuan et al.[41] A seed solution of citrate-capped nanospheres (NSps-cit) was prepared by adding 1.5 mL of 30 mM HAuCl$_4$·3H$_2$O (1% w/v) to 48.5 mL of boiling Milli-Q water and stirring (stirring at 400 rpm, 250 °C). After 10 s, 4.5 mL of a 38.8 mM sodium citrate solution was added to the reaction mixture. The boiling solution was stirred under heating for 15 min and then cooled at room temperature under magnetic stirring for 30 min. Citrate-capped nanostars (NSts-cit) were synthesized by adding 0.083 mL of 30 mM HAuCl$_4$·3H$_2$O (1% w/v), 10 μL of 1 M HCl, and 0.1 mL of the NSps-cit dispersion to 9.917 mL of Milli-Q water at room temperature under magnetic stirring. Then, 0.1 mL of 2.86 mM AgNO$_3$ and 0.05 mL of 0.1 M ascorbic acid were added simultaneously to the reaction mixture. The dispersion was stirred for 30−60 s, while its color turned from light red to dark gray (or blue). Afterward, NSts-cit were centrifuged for 40 min at 800 rcf, and the pellet was redispersed within distilled water. In order to obtain allylamine-conjugate NSts (NSts-AlAm), the citrate layer capping the NSts was replaced with a SH-PEG-COOH layer, so

as to expose reactive carboxylic moieties, which then could be conjugated with allylamine molecules. In particular, NSts-cit 1 nM was mixed with a 10 μM aqueous solution of PEG in a 9:1 volume ratio (molar ration 1:1000) and left under stirring at room temperature for 4 h. Subsequently, NPs-PEG were centrifuged at 25 °C and 2500 rpm for 30 min and redispersed in Milli-Q water. Carboxylic pendant moieties of NSts-PEG were activated by adding 0.4 mM EDC and 0.1 mM NHS to a 1.1 nM NSts-PEG dispersion. After 30 min at room temperature, 10 μL of allylamine aqueous solution with concentration ranging from 0.1 to 1 mM was added to the activated NSts-PEG dispersion to obtain final PEG/AlAm molar rations from 1:1 to 1:10. The reaction was stirred overnight, and then the allylamine-conjugated NPs (NSts-AlAm) were centrifuged at 2500 rpm for 30 min at 25 °C and finally redispersed in water.

Physicochemical Characterization of NPS. The plasmonic properties of the gold NP dispersion before and after functionalization were measured within the range 400−900 nm with a UV−vis−NIR spectrophotometer (Lambda 950 instrument, PerkinElmer, Waltham, MA, USA). The UV WinLab Software (PerkinElmer, Waltham, MA, USA) was used to acquire the spectra. The concentration of nanospheres (NSps) and nanostars (NSts) were determined according to the methods reported by Liu et al. and De Puig et al., respectively.[42,43] The hydrodynamic dimensions, polydispersity, and zeta-potential (ζ) were obtained through dynamic light scattering (DLS) analyses, which were performed with a Zetasizer Nano series ZS90 (Malvern, Worcestershire, UK). The measurements were performed with a fixed scattering angle of 90°, at 25 °C. Each sample was measured three times, and each measurement consisted of at least 30 acquisitions and of 30−100 acquisitions for ζ measurements. Cumulant methods were applied to autocorrelation functions to measure the mean hydrodynamic diameter and polydispersity. The NP morphology in terms of size and shape was characterized by transmission electron microscopy (Thermo Scientific Talo F200X equipped with a Ceta 16 M camera, using a single tilt sample holder and with a 4 in-column SDD Super-X energy-dispersive X-ray spectroscopy (EDX) detectors for 2D/3D chemical characterization). The endogenous fluorescence signal of allylamine was exploited to attest its conjugation to NPs through a fluorescence assay that was performed in a 96-well plate, using a microplate reader (FLUOStar Optima, BMG Labtech, Ortenberg, Germany). Measurements were repeated 10 times at 25 °C with a 2934 gain, a 320−10 nm excitation filter, and a 420−10 nm emission filter. AlAm successful conjugation of AlAm was also confirmed by Raman spectroscopy. Raman spectra before and after AlAm conjugation were collected with a conventional micro-Raman setup (XploRA PLUS Confocal Raman Microscope, Horiba, Japan), consisting of a 785 nm laser and a spectrometer with a focal length of 500 mm equipped with a 600 lines/mm grating. The incident laser power on the sample was about 20 mW. The scattered light was detected by a CCD camera operating at about 350 K. Raman-SERS spectra were recorded within the wavenumber range of 600−1800 cm^{-1}, with an acquisition time of 30 s. The measurements were repeated twice for spectral averaging. To avoid spurious signals, calcium fluoride Raman slides (CaF$_2$, Crystan) were used as the substrates. In order to extract the Raman signal of interest, fluorescence and background signals were subtracted from the acquired raw spectra, using SpectraGryph 1.2—spectroscopy software. All data and spectra were analyzed with the software Origin.

Preparation of PEGDA-Based Photocurable Mixtures. The photopolymer formulations were prepared by mixing the bifunctional oligomer PEGDA with the PI TPO-L. The latter was added at a 4% total weight of the resin (wt %), according to optimization studies previously performed.[24] In order to tune the number of photons absorbed by the PI and thus control the penetration depth of the 405 nm laser used for photostructuring, the BY dye was added to the hydrogel at various concentrations (from 0.1 to 0.5 wt %). Both the liquid TPO-L and powdered BY dye exhibited high solubility in PEGDA and absorption at the monochromatic emission wavelength (405 nm) of the laser (Figure S1). The photocurable functional composites were obtained by diluting the NSts within the PEGDA-BY matrix at different concentrations, with the range 5−100 nM. All the

dilutions were adjusted to have the same amount of water. Homogenous dispersions were obtained by stirring the solution for 2 h at room temperature.

SLA Printability of PEGDA-Based Mixtures. A benchtop SLA printer (XFAB2500HD, Digital Wax Systems, Italy) working in laser-scanning configuration (Figure S2) equipped with a monochromatic 405 nm laser source (Solid State BlueEdge BE-1500A/BE-1500AHR) with an emitting output power of 30 mW and a beam diameter of 50 μm was used. According to the standard procedure,[13,24,39] the "wedgeplot" method adapted from the diagnostic Windowpane technique was exploited to determine the depth of penetration D_p and the critical energy E_c of the varied formulations. Briefly, for each formulation, single-layer rectangular samples (10× 20 mm) were photopolymerized in the absence of the printing platform. Varied laser speeds were used to deliver different energy doses, resulting in different values of layer thickness (C_d). The average exposure E_{av} (mJ/cm^2) was calculated as

$$E_{av} = P_l/V_sH_s \tag{1}$$

where P_l is the laser power (30 mW), h_s is the laser line spacing (0.05 mm), and V_s is the laser scanning speed. The latter was set within the range 50−3000 mm/s, by using the DWS proprietary software Fictor (DWS systems, Italy). The polymerized samples were rinsed with ethanol to remove unreacted material, and their thickness C_d was measured with a digital micrometer in 3 different areas. Each composition was measured thrice. Then, according to Jacob's equation

$$C_d = D_p\ln(E_{av}/E_c) \tag{2}$$

$$C_d = D_p\ln E_{av} - \ln E_c \tag{3}$$

that can be developed as the "Jacob's working curve" for each formulation was obtained as a semilogarithmic plot of experimental C_d against set E_{av}. The slope and the x-axis intercept of the logarithmic-linear plot represent the penetration depth D_p and the critical exposure E_c, respectively.[44,45]

Rapid Prototyping of the Scaffolds. 3D millimetric cylindrical scaffolds (5−10 mm in height and 5−10 mm in diameter) and rectangular-based scaffolds (5−10 mm in height and 5−10 mm in width) with average pores size in the range 200−800 μm were designed using "Solidworks" software (Dassault Systems, France). Prior to the printing step, the 3D virtual models were reoriented on the building platform by using 3D parametric software Nauta + (DWS systems). Then, Nauta-processed files were loaded to Fictor (DWS systems), the commercial software machine that directly controls the 3D printer and performs the slicing operation according to the user-imposed building parameters that were adjusted considering the D_p and E_c values obtained for each SLA formulations as explained above. High-resolution scaffold printing was achieved within 20 min with the benchtop SLA printer mentioned above, characterized by 50 μm (laser spot diameter) and 10 μm of lateral and vertical resolution, respectively, setting up between 3000 and 5000 mm/s of laser speed, 25 and 50 μm of layer thickness, and 50 μm of hatching. At the end of the printing process, printed structures were rinsed with ethanol to remove unreacted materials, blown with nitrogen, and further irradiated for 30 min in a dedicated curing unit to accomplish the total polymerization conversion. Optical microscopy (OM) images were taken to check the structural integrity of the features.

■ MECHANICAL CHARACTERIZATION

Loss (G'') and storage (G') modulus and the tan δ value (tan δ = G''/G') were determined by dynamic mechanical analyses (DMA) that were performed with a DMA8000 Triton PerkinElmer instrument working in tensile configuration in the range from −60 to + 40 °C with a ramping rate of 5 °C/min at a frequency of 1 Hz. The samples used for DMA were rectangular films (5 mm × 10 mm) of approximately 200 μm thickness obtained by SLA laser scanning of adjacent lines. The
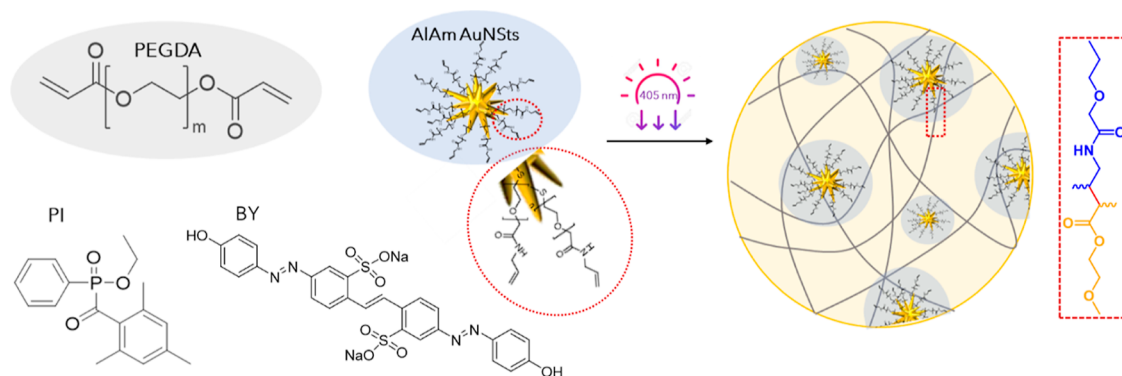
Figure 1. Scheme reporting the chemical structures of the components used to develop the photopolymer and photocomposite formulations. The scheme highlights the copolymerization occurring between the photoreactive pendant moieties of engineered NSts with end-chain reactive groups from PEGDA.
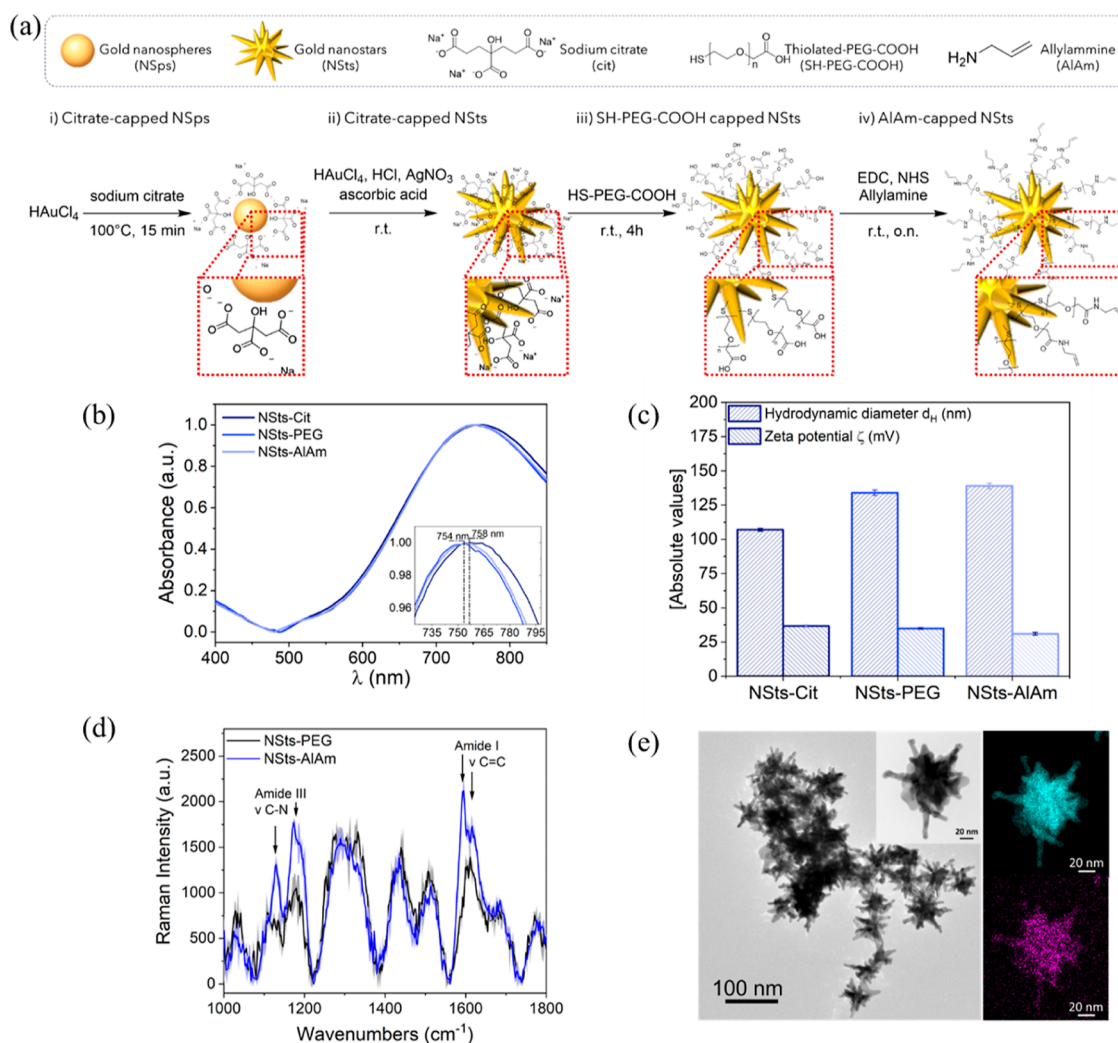
Figure 2. (a) Scheme reporting the steps of the NSts synthesis, PEGylation process through ligand exchange, and final assembly of allylamine via peptide bond formation. (b) UV−vis absorption spectra, (c) size distribution, and ζ potential for NSts-cit, NSts-PEG, and NSts-AlAm. (d) Raman spectra of NSts-PEG and NSts-AlAm conjugates. (e) TEM images of NSts-AlAm. The EDX maps reported in the insets show the elemental distribution of Au atoms (light-blue) and N atoms (violet) from allylamine.

swelling capability of the hydrogels at varied NP contents was studied by incubating 3D printed samples at 25 °C in PBS and weighing the swollen samples when at equilibrium after careful removal of excess liquid. The swelling ratio (SR) was calculated as $SR = (W_s - W_d)/W_d \times 100$ where W_s is the

weight at the swollen equilibrium and W_d is the weight of the dried sample. Then, the extent of mass swelling $q_M = W_s/W_d$ was used to determine the cross-linking density $v_{FR} = \rho_p/M_c$ of the hydrogels, which is correlated to their mechanical strength, by applying the approximate expression of the Flory−Rehner

equation valid for a network with a low degree of cross-linking swelling in a good solvent (as the case of hydrogels in water)[46,47]

$$q_e^{5/3} \cong \frac{M_c}{\rho_p V_1}\left(\frac{1}{2} - \chi\right) \tag{4}$$

where M_c is the average molecular weight between cross-links, V_1 is the molar volume of the solvent ($18\ \mathrm{cm^3\ mol^{-1}}$), ρ_p is the density of the dry polymer ($1.12\ \mathrm{g\ cm^{-3}}$), x is the Flory polymer–solvent interaction parameter (estimated to be 0.426 for PEGDA),[48] and q_e is the volumetric SR determined from q_M according to the following

$$q_e = 1 + \frac{\rho_p}{\rho_s}(q_M - 1) \tag{5}$$

with ρ_s the water density.

SERS Performances of Scaffolds. To preliminarily assess the SERS performances of SLA-printed structures with embedded NPs, the samples were immerged overnight in aqueous solution of MBA at decreasing concentration from 10^{-3} to 10^{-9} M. Then, the substrates were dried to remove excess of solution, placed on a calcium fluoride slide, and covered with a drop of water to prevent samples' drying during the acquisitions. Then, Raman spectra were randomly acquired using the micro-Raman setup (XploRA PLUS Confocal Raman Microscope, Horiba, Japan) excited through a 10× Nikon objective with a 785 nm laser. Spectra were collected and analyzed as reported above.

Cell Cultures and Imaging. Human immortalized HeLa cells were used to assess the biocompatibility of 3D printed scaffolds (with and without NPs). First, the structures were thoroughly washed with PBS for 48 h to release the excess of potentially cytotoxic BY dye and sterilized under UV-light for 25 min. To improve cell adhesion, the scaffolds were immerged in a fibronectin solution (0.7 mg/mL) for 24 h and left to dry for another 24 h. Cells were cultured in DMEM supplemented with 10% FBS, 1 mM glutamine, and 1% P/S solution in a humidified atmosphere at 37 °C and 5% CO_2 and grown until they reached 90% confluence. Cells were then plated onto 3D printed scaffolds in 24-well plates at 150,000 cells/well density and incubated for a total of 20 days with medium freshly replaced every day. At 5, 13, and 20 days, the scaffolds were incubated with 5 μg/mL WGA-594 (used for cell membrane staining) for 30 min at 37 °C and the WGA-594-derived fluorescence was then analyzed after excitation at 561 nm using a Nikon Eclipse TE300 C2 laser scanning confocal microscope (Nikon, Tokyo, Japan) and a Plan Fluor 20 × 0.75 NA water immersion objective. A series of optical sections (1024 × 1024 pixels) was taken and analyzed by using ImageJ software. All settings, including pinhole diameter, detector gain, and laser power, were kept constant for each analysis.

RESULTS AND DISCUSSION

The first aim of the present study was the development of novel laser-curable photocomposites doped with gold NPs for the high resolution SLA printing of 3D millimetric scaffolds exhibiting double functionalities of cell support and embedded SERS-sensing applications. To this end, a biocompatible photocurable mixture was obtained by doping PEGDA with a photoinitiator (PI) and PI-competing additives such as organic dyes, whose content was optimized to finely control the printing procedure. Then, the PEGDA mixtures were

further enriched with plasmonic gold NPs that were properly engineered (i) to maintain the colloidal stability at varied pH; (ii) to guarantee homogeneous distribution upon mixing with PEGDA, and (iii) to have photoreactive pendant moieties for covalent trapping in the hydrogel matrix by light-induced copolymerization (Figure 1).

To the best of our knowledge, we reported on a new straightforward protocol where NPs are engineered with C=C groups by implementing first a standard ligand-exchange process to attach a PEG-derived bifunctional ligand. This ligand contains thiols for covalent grafting to the gold surfaces [addressing (i) and (ii)] and a carboxyl end-chain groups for further conjugation with the −NH$_2$ amino group of allylamine (AlAm) through peptide bond formation (Figure 2a). The C=C groups from AlAm participated in the light-induced polymerization to covalently trap the NPs in the matrix [addressing (iii)].[49] In particular, we focused on gold nanospheres (NSps) and, more interestingly, on gold nanostars (NSts) recognized as highly performing SERS substrates with respect to NSps due to their anisotropic morphology constituted by a spherical core with sharp nanometric cylindrical-shaped tips randomly protruding. These protrusions form numerous intrinsic tip-to-tip gaps working as Raman "hot spots", specific sites on plasmonic surfaces where the electromagnetic radiation is localized and strongly amplified.[35] According to the scheme reported in Figure 2a, star-shaped particles were synthesized starting from the spherical seeds [step (i), NSts-cit] (Figure S3), immediately followed by an exchange ligand process with bifunctional SH-PEG-COOH molecules [step (ii), NSts-PEG]. NSts-PEG were further conjugated to AlAm molecules [step (iii), NSts-AlAm] exploiting the formation of amide bonds (between −COOH derived from PEG and NH$_2$ from allylamine) through standard carbodiimide chemistry. Extinction spectra reported in Figure 2b demonstrated that the covalent anchoring of PEG followed by the conjugation of AlAm molecules was successfully accomplished without altering the complex branched morphology of the NSts and thus their plasmonic properties. Indeed, the small blue shift observed in the maximum of absorbance for NSts-PEG and for NSts-AlAm is ascribable to the change of chemical environment at the gold surface due to PEG and AlAm conjugations that directly affects the local refractive index and therefore the plasmonic properties. As expected for each functionalization step, the hydrodynamic diameter of NSts was observed to increase from 107 ± 1 nm immediately after the synthesis to 134 ± 2 nm for NSts-PEG and from 139 ± 2 nm for NSts-AlAm. At the same time, switching from citrate to PEG and then AlAm surface molecules, the net negative charge of NSts decreased due to the lower content of carboxyl groups, with zeta potential values (ζ) from −36.7 ± 0.8 mV for NSts-cit to −34.9 ± 0.8 mV for NSts-PEG and −31 ± 1 mV for NSts-AlAm (Figure 2c). AlAm-conjugation to the NSts-PEG surface was further assessed through Raman-SERS measurements. Figure 2d reports vibrational peaks from NSts-AlAm (blue line) and NSts-PEG (black line) as a reference. Spectra are almost completely overlapped in those regions referring to PEG bonds (vC−H and vC−C), while substantial differences could be observed mainly between 1100 and 1200 and 1580−1600 cm^{-1}. As expected, in the presence of AlAm molecules attached to the NSts surface, C−N and C=C bond stretching as well as amide I and amide III become predominant peaks, which are intrinsic to allylamide, confirming the conjugation. Following previous results,[50] the

Table 1. Composition and Curing Conditions of the PEGDA-Based Mixtures Tested for SLA Printability

PEGDA-based mixtures[a]	PI [wt %]	dye BY [wt %]	NPs [nM]	stirring [rpm]	λ [nm]	T_{curing} [°C]
PEGDA + PI + BY		0−0.5				
PEGDA + PI + NPs	4		5−20	300	405	T_{amb}
PEGDA + PI + BY + NPs		0.25−0.5	5−100			

[a]Water content <10 vol % for all the mixtures.
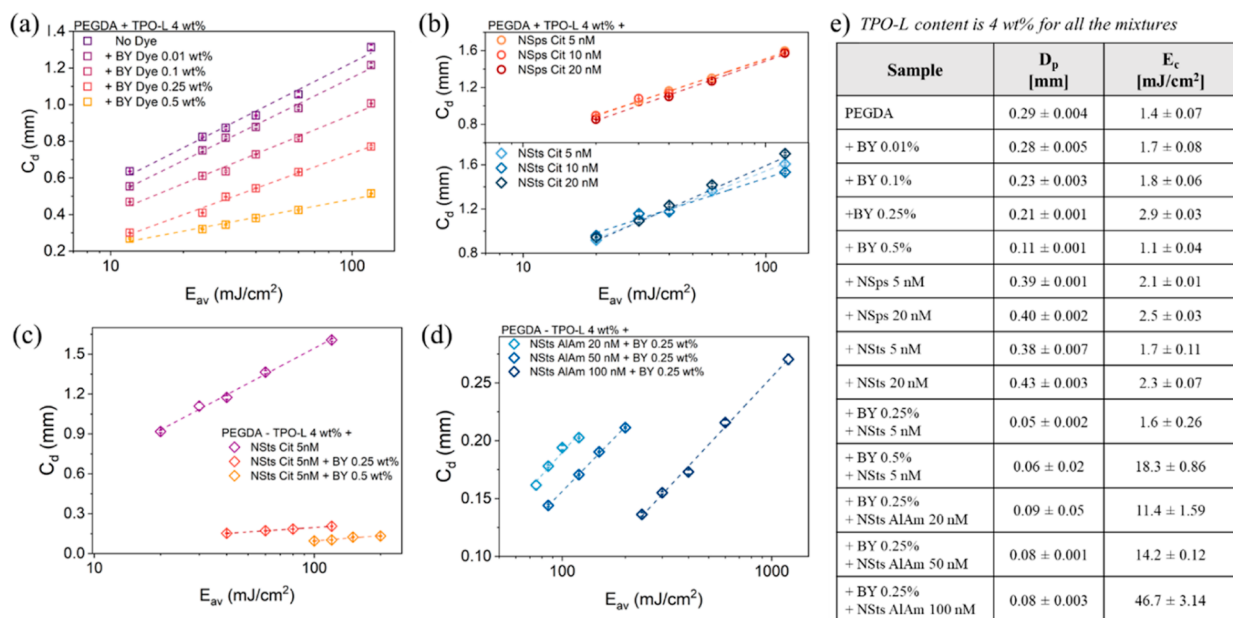
Figure 3. Curing depths C_d for PEGDA-based formulations were plotted against the average energy doses E_{av} giving a straight line (the "Jacob's working curve"), whose slope represents the penetration depth D_p and whose x-intercept is the critical energy E_c. The laser working curves were experimentally determined for (a) PEGDA at varied BY dye contents, (b) PEGDA at varied NP contents, (c) PEGDA at fixed NP content with varied BY dye contents, and (d) PEGDA at fixed BY dye content with NP content increasing until 100 nM. (e) Table resuming the D_p and E_c values determined for the varied PEGDA-based formulations.

intrinsic fluorescence properties of AlAm could also be exploited to attest AlAm conjugation. Indeed, the AlAm fluorescence spectrum is characterized by a broad absorbance peak centered at 330 nm with an emission peak at around 390 nm (Figure S4a). Finally, TEM images revealed that the highly branched NSts morphology was retained upon AlAm-functionalization; the latter also confirmed by EDX chemical composition maps, thereby ensuring retention of their morphology-dependent activities, such as SERS resonant one (Figure 2e).

Then, NSts were mixed with a PEGDA mixture to check the potential scattering and/or absorption effect of NPs on laser penetration and the effect on the SLA printing resolution. Table 1 resumes the main components and conditions of the PEGDA-based mixtures tested for SLA printability.

Before testing NP-doped composites, the SLA behavior of pristine PEGDA was optimized by adding PI-competing dye (BY) in order to decrease the sensitivity D_p and the critical energy E_c of the formulation, thus guaranteeing satisfactory fabrication conditions in terms of resolution and printing speed, respectively. To this aim, while the content of the PI was kept at 4 wt %, to further reduce the D_p, an increasing amount of BY dye adsorbing in the wavelength 350−500 nm was added, and the corresponding D_p and E_c were determined experimentally by plotting the laser working curve for each formulation according to Jacob's equation (eq 2). As expected, starting from the pristine PEGDA-TPO-L formulation, the slope of the laser working curve (corresponding to the D_p) was

observed to decrease by increasing the BY content with values down to 0.11 mm for 0.5 wt % BY, more than halved with respect to the starting PEGDA (Figure 3a). No significant variation or trend was observed for the E_c parameter that resulted lower with respect to data from the literature. This should guarantee fast photocurable polymerization and, from the fabrication point of view, high laser speed to be set for structures prototyping. Higher amounts of BY dye were not considered due to its limit of miscibility and to its potential cytotoxicity that (the dye is just physically trapped in the polymer matrix and could be released upon incubation in aqueous solution such as in cell cultures). PEGDA-TPO-L 4 wt % doped with BY 0.5% was selected as best-performing SLA-processable resin for scaffold fabrication and as the benchmark for comparison with NP-doped PEGDA formulations in terms of SLA printing parameters.

We then explored the influence of NPs, engineered with different capping agents, on the PEGDA SLA printability. As shown from the laser working curves reported in Figure 3b, no strong effect on laser confinement was obtained upon mixing pristine PEGDA with NPs in the 5−20 nM range, with D_p values ranging between 0.38 and 0.43 mm, almost doubled with respect to dye-doped PEGDA mixtures. The same trend was confirmed for PEG-stabilized NPs (Figure S5). This is probably due to the plasmonic peak of nanospheres (λ = 520 nm) and nanostars (λ = 780 nm) that does not match with the λ of the SLA-printer (λ = 405 nm) and thus they not compete with the PI in absorbing photons. Another criticism could be
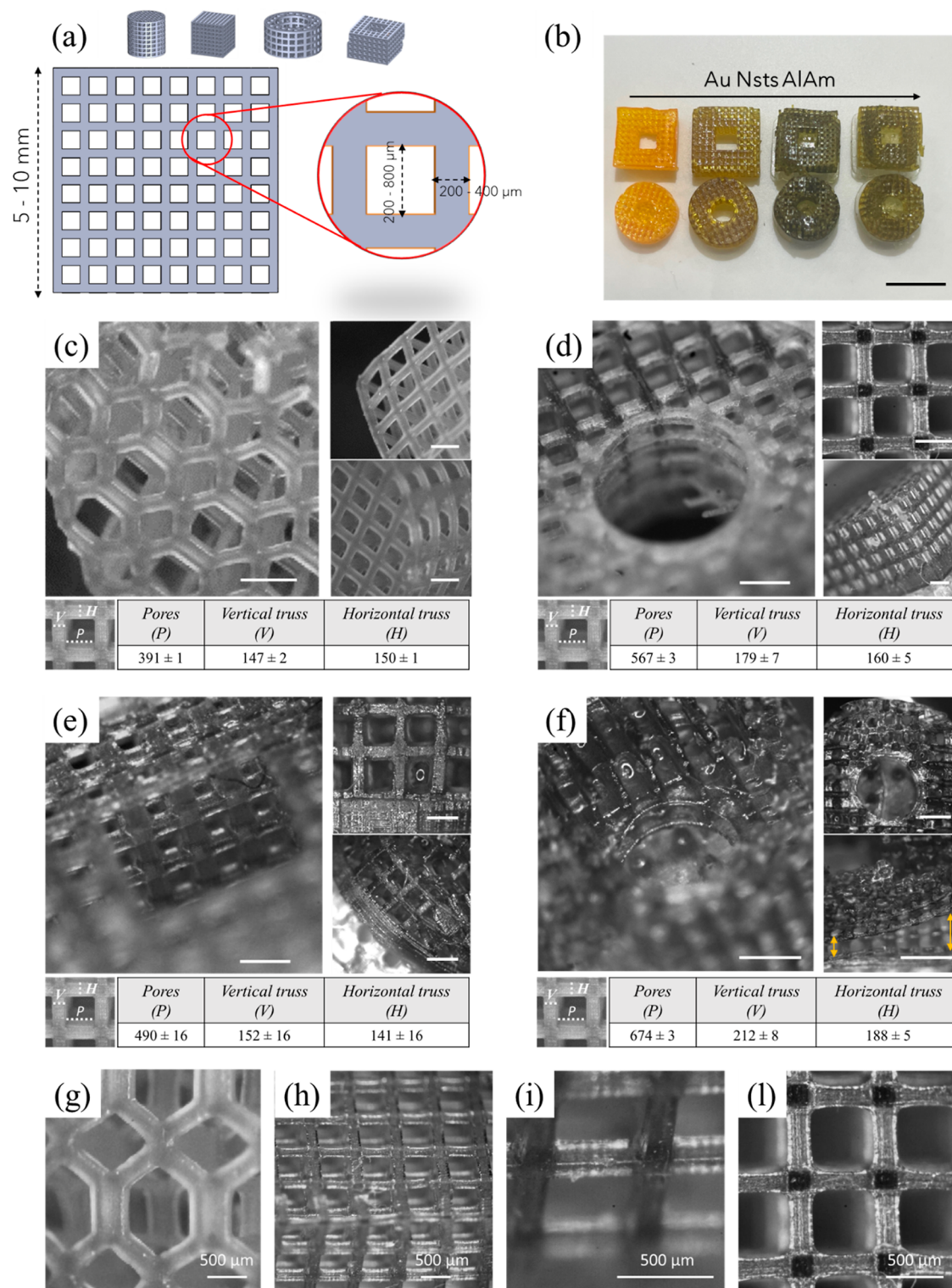
Figure 4. (a) Overall design of the circular- and rectangular-based millimetric scaffolds with internal porosity at the micrometric scale. (b) Photograph of the prototypes 3D printed at NSts AlAm increasing concentration. The scale bar is 10 mm. (c–l) OM images and mean dimensions of 3D models printed (c) without NPs and with NPs (d) 20 nM and (e) 50 nM attested that SLA printability was optimized with self-standing prototypes exhibiting good structural fidelity with well-defined pores. At (f) 100 nM NPs content, delamination of layers started to occur (red arrow). The scale bar is 1 mm for (c,f) and 500 μm for (d,e).

represented by the different amounts of water that were necessarily added to the PEGDA solution to have NPs at different dilutions. Indeed, the experimental laser working curves obtained for PEGDA/H$_2$O solutions at different ratios attested the D_p worsening (from 0.25 to 0.45 mm) upon

increasing the water content (Figure S6). This is probably due to the higher perfusion of hydrated PEGDA chains whose increased mobility could increase chain interactions and consequently the local density of light-reactive C=C involved in the photopolymerization process. Based on this exper-
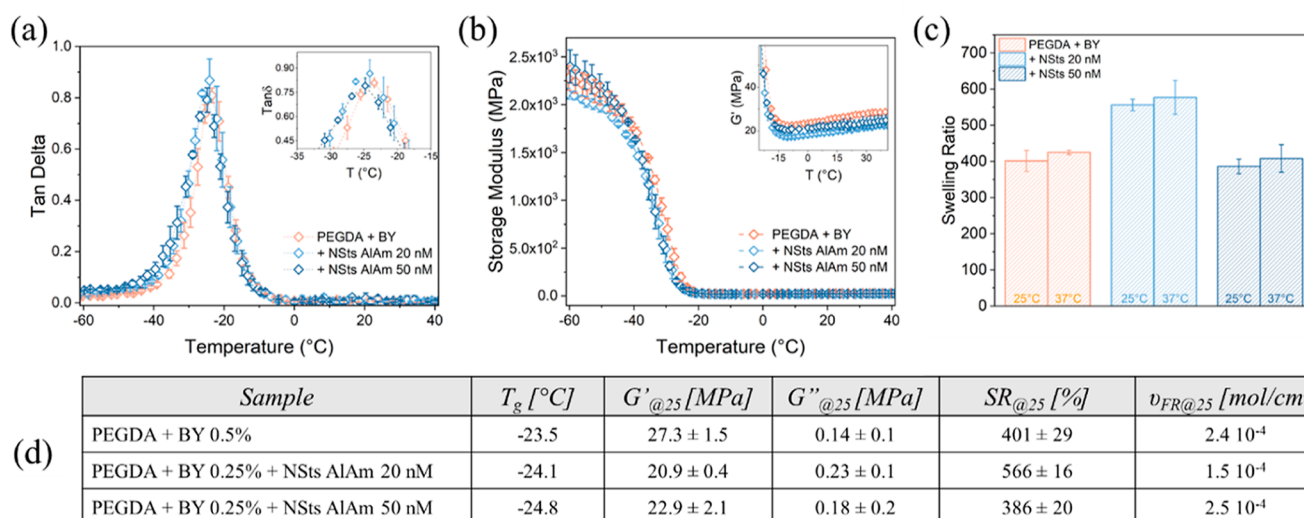
Figure 5. (a) Tan δ and (b) storage modulus G' of rectangular-shaped laser cured samples at increasing NP content measured by DMA. (c) Swelling behavior of PEGDA-based samples measured at 25 °C at increasing NP content. (d) Table resuming the main thermal and mechanical characteristics of the samples SLA-cured at varied NP contents.

Sample	T_g [°C]	$G'_{@25}$ [MPa]	$G''_{@25}$ [MPa]	$SR_{@25}$ [%]	$v_{FR@25}$ [mol/cm³]
PEGDA + BY 0.5%	-23.5	27.3 ± 1.5	0.14 ± 0.1	401 ± 29	2.4 10⁻⁴
PEGDA + BY 0.25% + NSts AlAm 20 nM	-24.1	20.9 ± 0.4	0.23 ± 0.1	566 ± 16	1.5 10⁻⁴
PEGDA + BY 0.25% + NSts AlAm 50 nM	-24.8	22.9 ± 2.1	0.18 ± 0.2	386 ± 20	2.5 10⁻⁴

imental evidence, all NP-PEGDA mixtures were formulated with the same amount of water that was kept lower than 10% with respect to the total volume of the formulations. In order to compensate for the effect of water on laser-induced photopolymerization, following previous results from pristine PEGDA, BY dye was further added to the NP-PEGDA mixtures. As expected, laser working curves acquired for NPs 5 nM attested that D_p values were drastically reduced of about an order of magnitude (from 0.4 to 0.05 mm) upon addition of BY dye (Figure 3c), thus confirming the key role played by the visible dye as PI-competitor in absorbing photons. Unlike pristine PEGDA formulations, where the BY dye optimal content resulted in 0.5 wt %, in the presence of NPs, BY dye content was set at 0.25 wt % because the experimental E_c values (18 mJ/cm²) obtained at BY 0.5 wt % meant that higher energy doses should be required to fully polymerize the formulation with a strong impact on laser speed and scaffold fabrication times. Once the contents of water and dye were optimized, in order to guarantee intrinsic SERS functionality to the 3D printed structures, the content of NSts-AlAm was pushed up to 100 nM.[32] As reported in Figure 3d, the slope of the laser working curves remained constant, with D_p values around 0.08 mm, slightly increased with respect to the D_p at NSts 5 nM. This behavior could be due to the steric incumbrance of NPs among polymer chains and to the increased density of functional light-reactive groups locally irradiated by the laser in the resin that resulted in a thicker single-line layer.[12] On the other hand, E_c values increased until 46 mJ/cm² upon increasing NSts AlAm to 100 nM. This trend was probably due to the higher density of NPs whose photons shielding effect could obstruct light propagation. In these conditions, slower laser scanning rates would be necessary to print a structure as more energy would be required to reach the gel point, thus impacting on the speed of the overall printing process.[24,51] Proof-of-concept scaffold prototyping reported later further attested that the 100 nM NSts formulation could hardly be 3D printed with our SLA-apparatus.

Once the SLA behavior of the BY dye- and NPs-AlAm-doped PEGDA resins was optimized, millimetric self-standing scaffolds of varied designs were successfully SLA-printed within 20 min with controlled porosity in the 200−800 μm range (Figure 4a). For each formulation, the layer thickness was set to be smaller than the penetration depth in order to guarantee adhesion between consecutive layers while avoiding delamination.[52] The laser speed was set to give enough energy for the photocomposites to reach the gel point and to guarantee stability of fresh 3D printed layers while avoiding overexposure that could alter the geometrical features of the 3D printed parts (e.g., closed porosity in the scaffolds). For BY dye-doped PEGDA, the layer thickness and laser speed were set at 50 μm and 5000 mm/s, respectively. Upon NSts-AlAm addition, slower printing processes were requested because a higher energy dose per area unit was needed. Layer thickness was lowered to 25 μm and laser speed was lowered down to 3000 mm/s for 20 nM content and to 2000 mm/s at higher NP contents. 3D printed structures showed a homogeneous color typical of BY dye, turning to green-blue in the presence of NPs, demonstrating that NPs remained stable and well dispersed in the matrix (Figure 4b). OM images (Figure 4c−l) revealed the excellent physical integrity of SLA-scaffolds with fully interconnected pore networks and repetitive architecture throughout the structures. Furthermore, micrometric printing resolution was successfully achieved with features down to 100 μm, to date never reported for PEGDA doped with NPs and reported for PEGDA doped with dye but only when exploiting a highly expensive two-photon setup.[53] As previously mentioned, delamination of layers was observed only at the highest NP concentration as a consequence of the E_c of about 46 mJ/cm² (Figure 4f, inset). This could be overcome by further lowering the laser speed and/or layer thickness. The mechanical properties and structural stability of 3D printed parts were characterized to check the influence of the NPs. To this end, DMA analyses were performed on 200 μm rectangular-shaped samples fabricated by exploiting the same SLA-fabrication processes adopted for the scaffolds. Results from DMA analysis highlighted that no crucial impact on the glass thermal transition (T_g) as well as on the mechanical properties of the photopolymers and photocomposites was observed. More in detail, T_g values were observed to range between −23 and −25 °C (Figure 5a) with no clear
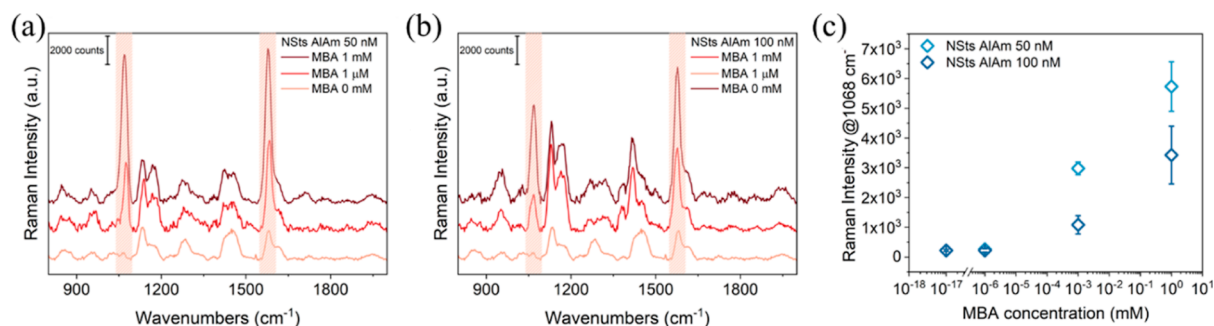
Figure 6. Average SERS spectra obtained upon laser irradiation of the scaffolds containing (a) NSts AlAm 50 nM and (b) NSts AlAm 100 nM and incubated with a decreasing concentration of MBA. (c) Raman intensity of the 1069 cm^{-1} peak obtained for NSts AlAm 50 and 100 nM as a function of MBA concentration.
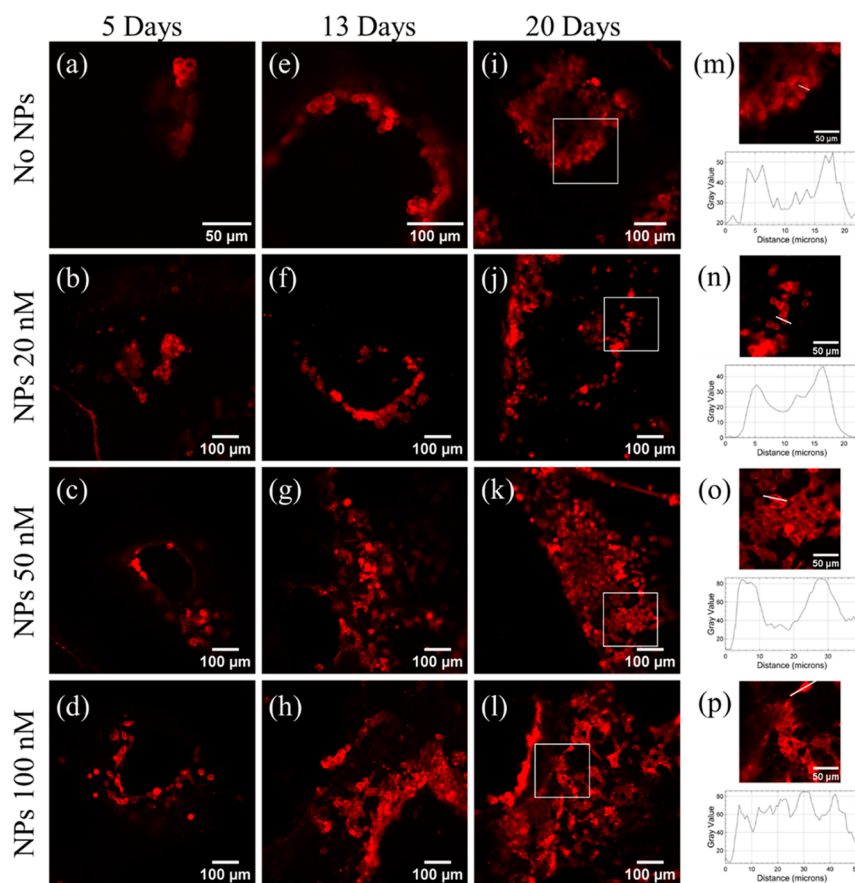
Figure 7. Confocal microscope images of HeLa cells seeded onto SLA-printed scaffolds with NPs at varied concentrations after 5 days (a−d), 13 days (e−h), and 20 days (i−l) of culture. (m−p) Magnified images showing the changes in morphology from rounded to highly stretched observed as a function of NP loading in PEGDA matrices. The graph reports the line profiles of fluorescence intensity of a single cell marked white in the inset.

dependency on NP concentration and with values corresponding with values from the literature reported for pure UV-cured PEGDA. Data from the literature were also confirmed for the storage modulus with slightly higher values obtained for PEGDA-BY photopolymer ($G' \approx 27$ MPa) with respect to photocomposites with NSts AlAm 20 nM ($G' \approx 21$ MPa) and 50 nM ($G' \approx 23$ MPa) (Figure 5b). The slight G' decrease for NSts-doped formulations could be due to the 10% water content as attested from other works showing the trend of decreasing PEGDA mechanical properties upon increasing the water content of PEGDA formulations. These results attested that PEGDA mechanical properties were retained with no

degradation phenomena or radicals quenching induced by metal NPs thermal effect during SLA laser irradiation.[54,55] Finally, all samples showed gel-like behavior, with G'' values lower than G' values for all the investigated ranges of temperature (Figure S7).

The trend observed for G' with values slightly increasing in the presence of NPs was confirmed by the SR measurements (Figure 5c) that were performed by incubating 3D printed scaffolds in PBS until their swelling equilibrium. Measurements performed at different temperatures presented no significative variation with slightly higher SR values for incubations at 37 °C in accordance with data from the literature[23,48,56] Finally, as

a proof of concept, the real possibility to exploit NPs embedded within the 3D printed scaffolds as highly efficient SERS-nanosensors for Raman enhancement due to NP-localized surface plasmon resonance was explored. To this end, the scaffolds with 50 and 100 nM NSts AlAm concentrations were immerged in MBA Raman reporter aqueous solution for 1 h and randomly irradiated with a 785 nm laser source (in resonance with the plasmonic peak of NSts). The Raman-SERS signal was collected to check the differences in physical adsorption of MBA while gradually reducing its concentration down to 1 nM. As shown from the spectra reported in Figure 6, the intensity of the MBA characteristic Raman peaks at 1069 and 1577 cm^{-1} were observed to increase as a function of MBA content with signal intensity higher for NSts 50 nM, or at least comparable, with respect to NSts 100 nM (Figure 6a,b). Furthermore, MBA was clearly detectable for concentrations down to 1 μm at least an order of magnitude lower with respect to the main reported example where NSts-PEG are embedded in a polymer matrix for SERS-sensing purposes.[32] The lower signal intensities obtained at higher NP content could be due to the resulting lower transparency of scaffolds that could limit the laser penetration and thus the irradiated sample volume (Figure 6c). Finally, successful preliminary results attested that the integration of NPs within the photopolymer matrix combined with the laser-based SLA printing process does not alter the Raman enhancement capability of the NSts and provides an interesting perspective for the rapid prototyping of cells support with embedded noninvasive SERS sensors potentially exploitable for the real-time monitoring of cell culture conditions (e.g., by the selective revealing of secreted biomolecules).

To further attest the feasibility of 3D printed structures as advanced scaffolds with a double role of supporting 3D cell growth and monitoring through spectroscopic techniques, their biocompatibility was evaluated upon culturing with HeLa cells for 20 days. While the biocompatibility of PEGDA and PEG-decorated NPs has been widely reported, here we tested the biocompatibility of novel NP-constructs engineered with allylamine whose unreacted residues could potentially be cytotoxic. After properly washing the scaffolds to remove the excess of BY dye, HeLa cells were seeded onto sterilized structures fabricated with varying concentrations of NSts-AlAm (0, 20, 50, and 100 nM). To study the growth and rearrangement of the HeLa cells within the 3D samples, confocal microscope images were acquired after staining cell membranes. Viable HeLa cells were observed to attach and proliferate in all the samples, thus attesting the compatibility of the SLA-printed structures (Figure 7). As shown in Figure 7a–d, despite the high density used for seeding, after 5 days, few HeLa cells were observed to attach along the open microporosity of the scaffolds with slight increase in cell colonies upon increase in NP loading. The lower number of cells at day 5 is probably due to the fact that the scaffolds are not perfectly attached to the bottom of the multiwell plate, thus making it harder for the cells to migrate and climb in the 3D structures. Another interesting aspect is the different morphology of HeLa that seemed more rounded for pristine PEGDA samples and got more stretched upon increasing in NSts content with longitudinal dimension increasing from about 15 to 30 μm. This behavior was accentuated at day 13 (Figure 7e–h) and became clearly visible after 20 days of culture (Figure 7i–l), with HeLa showing the typical rhomboid–tetrahedral shape

for NSts 50 and 100 nM, as highlighted in the inset (Figure 7m–p).[57] This result preliminarily demonstrated that cells preferentially interacted with the substrates with NPs, probably inducing cell-cytoskeleton rearrangements toward a physiological HeLa shape, a crucial point when addressing tissue engineering applications. Furthermore, at higher NSts content, cells were observed to migrate from the internal micropores and to colonize the whole structure with the formation of uniform and partially interconnected layer completely covering the scaffold truss (Figure 7k,l). On the contrary, without NPs, cell proliferation was not inhibited but remained confined within the internal pores (Figure 7i).

CONCLUSIONS

In conclusion, novel gold NP-hydrogel photocomposites were successfully optimized to be processed at high resolution by a low-cost benchtop SLA apparatus for the fabrication of 3D scaffolds. 3D-printed gold-decorated structures guaranteed cell supporting and proliferation as well as potential for real-time sensing of analytes secreted in the cultures through SERS-based optical approaches. To this end, a novel allylamine-conjugated NP construct characterized by highly branched star-shaped morphology was engineered to expose photocurable pendant moieties on the surfaces, thus guaranteeing covalent trapping via light-induced copolymerization as well as colloidal stability upon mixing with a PEGDA matrix. The effect of NP inclusion on 3D printing resolution was studied, and by optimizing the NP content, PEGDA formulations were tailored for the SLA-prototyping of millimetric scaffolds with highly defined and fully interconnected microporosity at improved resolution with respect to the literature and avoiding the use of expensive 2PP fabrication processes. Then, the potential exploitation of embedded NPs as an integrated SERS platform for real-time biosensing was successfully attested through the detection of a proof-of-concept Raman active molecule. Among all formulations, 50 nM NP content gave the best compromise between SLA printability, enabling the printing of structures down to 150 μm and retaining intrinsic SERS performances, with sensing capabilities between 1 nM and 1 μM. Finally, cell studies not only confirmed the biocompatibility of SLA-printed plasmonic scaffolds but also preliminary demonstrated that the presence of NPs at higher content could induce cells' physiological morphologic rearrangements, a crucial point when addressing tissue engineering applications. A deeper insight into the quantitative effect of scaffolds on cell proliferation will be object of further investigations.[58] Indeed, the integration of metallic NPs within biocompatible photopolymers processable at high resolution by low-cost laser-based 3D printing techniques addresses the current need in 4D bioprinting for novel functional materials engineered to describe the native tissues *in vitro* more accurately. Future developments of this work will focus on further engineering of NPs with the dual scope of detecting useful biomarkers for monitoring culture progression as well as culture and to deliver chemical or physical stimuli to the cells.

ASSOCIATED CONTENT

Ⓢ Supporting Information

The Supporting Information is available free of charge at https://pubs.acs.org/doi/10.1021/acsabm.4c00379.

UV−visible spectra of additive compounds; scheme of the working principle for SLA printer working in the

laser-scanning configuration; UV−vis, DLS, and TEM of citrate-capped NSps; absorption and emission spectra of allylamine-conjugated NPs; laser working curves for PEGDA-PEGylated NPs and for PEGDA/H$_2$O formulations at different ratios; and G' and G'' moduli for PEGDA-NP formulations (PDF)

■ AUTHOR INFORMATION

Corresponding Author

Caterina Credi − *European Laboratory for Non-Linear Spectroscopy, University of Florence, Sesto Fiorentino 50019, Italy; National Institute of Optics−National Research Council, Sesto Fiorentino 50019, Italy;* orcid.org/0000-0003-4565-5214; Email: caterina.credi@ino.cnr.it, caterina.credi@gmail.com

Authors

Isabel Ventisette − *Department of Industrial Engineering, University of Florence, Florence 50121, Italy*

Francesco Mattii − *European Laboratory for Non-Linear Spectroscopy, University of Florence, Sesto Fiorentino 50019, Italy*

Caterina Dallari − *European Laboratory for Non-Linear Spectroscopy and Department of Physics and Astronomy, University of Florence, Sesto Fiorentino 50019, Italy; National Institute of Optics−National Research Council, Sesto Fiorentino 50019, Italy;* orcid.org/0000-0003-1787-0697

Claudia Capitini − *National Institute of Optics−National Research Council, Sesto Fiorentino 50019, Italy; Department of Physics and Astronomy, University of Florence, Sesto Fiorentino 50019, Italy*

Martino Calamai − *European Laboratory for Non-Linear Spectroscopy, University of Florence, Sesto Fiorentino 50019, Italy; National Institute of Optics−National Research Council, Sesto Fiorentino 50019, Italy;* orcid.org/0000-0002-4031-7235

Beatrice Muzzi − *Institute of Chemistry of Organometallic Compounds−National Research Council, Sesto Fiorentino 50019, Italy*

Francesco S. Pavone − *European Laboratory for Non-Linear Spectroscopy and Department of Physics and Astronomy, University of Florence, Sesto Fiorentino 50019, Italy; National Institute of Optics−National Research Council, Sesto Fiorentino 50019, Italy;* orcid.org/0000-0002-0675-3981

Federico Carpi − *Department of Industrial Engineering, University of Florence, Florence 50121, Italy*

Complete contact information is available at:
https://pubs.acs.org/10.1021/acsabm.4c00379

Author Contributions

[#]I.V. and F.M. contributed equally. The manuscript was written through contributions of all authors. All authors have given approval to the final version of the manuscript.

Notes

The authors declare no competing financial interest.

■ ACKNOWLEDGMENTS

■ REFERENCES

(1) Suuronen, E. J.; Sheardown, H.; Newman, K. D.; McLaughlin, C. R.; Griffith, M. Building in Vitro Models of Organs. *Int. Rev. Cytol.* **2005**, *244*, 137−173.

(2) Huh, D.; Hamilton, G. A.; Ingber, D. E. From 3D Cell Culture to Organs-on-Chips. *Trends Cell Biol.* **2011**, *21* (12), 745−754.

(3) Chan, V.; Zorlutuna, P.; Jeong, J. H.; Kong, H.; Bashir, R. Three-Dimensional Photopatterning of Hydrogels Using Stereolithography for Long-Term Cell Encapsulation. *Lab Chip* **2010**, *10* (16), 2062−2070.

(4) Bagheri, A.; Jin, J. Photopolymerization in 3D Printing. *ACS Appl. Polym. Mater.* **2019**, *1* (4), 593−611.

(5) Ashammakhi, N.; Ahadian, S.; Xu, C.; Montazerian, H.; Ko, H.; Nasiri, R.; Barros, N.; Khademhosseini, A. Bioinks and Bioprinting Technologies to Make Heterogeneous and Biomimetic Tissue Constructs. *Mater. Today Bio* **2019**, *1*, 100008.

(6) Jang, J.; Yi, H.-G.; Cho, D.-W. 3D Printed Tissue Models: Present and Future. *ACS Biomater. Sci. Eng.* **2016**, *2* (10), 1722−1731.

(7) Layani, M.; Wang, X.; Magdassi, S. Novel Materials for 3D Printing by Photopolymerization. *Adv. Mater.* **2018**, *30* (41), 1706344.

(8) Kufelt, O.; El-Tamer, A.; Sehring, C.; Schlie-Wolter, S.; Chichkov, B. N. Hyaluronic Acid Based Materials for Scaffolding via Two-Photon Polymerization. *Biomacromolecules* **2014**, *15* (2), 650−659.

(9) Nava, M. M.; Raimondi, M. T.; Credi, C.; De Marco, C.; Turri, S.; Cerullo, G.; Osellame, R. Interactions between Structural and Chemical Biomimetism in Synthetic Stem Cell Niches. *Biomed. Mater.* **2015**, *10* (1), 015012.

(10) Ovsianikov, A.; Mironov, V.; Stampfl, J.; Liska, R. Engineering 3D Cell-Culture Matrices: Multiphoton Processing Technologies for Biological and Tissue Engineering Applications. *Expert Rev. Med. Devices* **2012**, *9* (6), 613−633.

(11) Wang, Y.; Zhou, Y.; Lin, L.; Corker, J.; Fan, M. Overview of 3D Additive Manufacturing (AM) and Corresponding AM Composites. *Compos. Part A Appl. Sci. Manuf.* **2020**, *139*, 106114.

(12) Credi, C.; Levi, M.; Turri, S.; Simeone, G. Stereolithography of Perfluoropolyethers for the Microfabrication of Robust Omniphobic Surfaces. *Appl. Surf. Sci.* **2017**, *404*, 268−275.

(13) Credi, C.; Griffini, G.; Levi, M.; Turri, S. Biotinylated Photopolymers for 3D-Printed Unibody Lab-on-a-Chip Optical Platforms. *Small* **2018**, *14*, 1702831.

(14) D'Amora, U.; Ronca, A.; Raucci, M. G.; Lin, H.; Soriente, A.; Fan, Y.; Zhang, X.; Ambrosio, L. Bioactive Composites Based on Double Network Approach with Tailored Mechanical, Physico-Chemical, and Biological Features. *J. Biomed. Mater. Res. Part A* **2018**, *106* (12), 3079−3089.

(15) Li, H.; Tan, C.; Li, L. Review of 3D Printable Hydrogels and Constructs. *Mater. Des.* **2018**, *159*, 20−38.

(16) Kumar, S.; Tharayil, A.; Thomas, S. 3D Bioprinting of Nature-Inspired Hydrogel Inks Based on Synthetic Polymers. *ACS Appl. Polym. Mater.* **2021**, *3* (8), 3685−3701.

(17) Guo, A.; Zhang, S.; Yang, R.; Sui, C. Enhancing the Mechanical Strength of 3D Printed GelMA for Soft Tissue Engineering Applications. *Mater. Today Bio* **2024**, *24*, 100939.

(18) Kirchmajer, D. M.; Gorkin III, R.; in het Panhuis, M. An Overview of the Suitability of Hydrogel-Forming Polymers for Extrusion-Based 3D-Printing. *J. Mater. Chem. B* 2015, 3 (20), 4105−4117.

(19) Chimene, D.; Kaunas, R.; Gaharwar, A. K. Hydrogel Bioink Reinforcement for Additive Manufacturing: A Focused Review of Emerging Strategies. *Adv. Mater.* 2020, 32 (1), No. e1902026.

(20) Thomas, A.; Orellano, I.; Lam, T.; Noichl, B.; Geiger, M.-A.; Amler, A.-K.; Kreuder, A.-E.; Palmer, C.; Duda, G.; Lauster, R.; et al. Vascular Bioprinting with Enzymatically Degradable Bioinks via Multi-Material Projection-Based Stereolithography. *Acta Biomater.* 2020, 117, 121−132.

(21) Tomal, W.; Ortyl, J. Influence of a Non-Reactive Additive on the Photocuring and 3D-VAT Printing Processes of PEGDA: Complementary Studies. *Eur. Polym. J.* 2022, 180, 111588.

(22) Hossain Rakin, R.; Kumar, H.; Rajeev, A.; Natale, G.; Menard, F.; Li, I. T. S.; Kim, K. Tunable Metacrylated Hyaluronic Acid-Based Hybrid Bioinks for Stereolithography 3D Bioprinting. *Biofabrication* 2021, 13 (4), 044109.

(23) Hakim Khalili, M.; Zhang, R.; Wilson, S.; Goel, S.; Impey, S. A.; Aria, A. I. Additive Manufacturing and Physicomechanical Characteristics of PEGDA Hydrogels: Recent Advances and Perspective for Tissue Engineering. *Polymers* 2023, 15, 2341.

(24) Credi, C.; Fiorese, A.; Tironi, M.; Bernasconi, R.; Magagnin, L.; Levi, M.; Turri, S. 3D Printing of Cantilever-Type Microstructures by Stereolithography of Ferromagnetic Photopolymers. *ACS Appl. Mater. Interfaces* 2016, 8 (39), 26332−26342.

(25) Urie, R.; Ghosh, D.; Ridha, I.; Rege, K. Inorganic Nanomaterials for Soft Tissue Repair and Regeneration. *Annu. Rev. Biomed. Eng.* 2018, 20, 353−374.

(26) Dvir, T.; Timko, B. P.; Kohane, D. S.; Langer, R. Nanotechnological Strategies for Engineering Complex Tissues. *Nat. Nanotechnol.* 2011, 6 (1), 13−22.

(27) Yadid, M.; Feiner, R.; Dvir, T. Gold Nanoparticle-Integrated Scaffolds for Tissue Engineering and Regenerative Medicine. *Nano Lett.* 2019, 19 (4), 2198−2206.

(28) Xue, K.; Wang, F.; Suwardi, A.; Han, M.-Y.; Teo, P.; Wang, P.; Wang, S.; Ye, E.; Li, Z.; Loh, X. J. Biomaterials by Design: Harnessing Data for Future Development. *Mater. Today Bio* 2021, 12, 100165.

(29) Sharma, B.; Frontiera, R. R.; Henry, A.; Ringe, E.; Van Duyne, R. P. SERS: Materials, applications, and the future. *Mater. Today* 2012, 15 (1−2), 16−25.

(30) Dallari, C.; Lenci, E.; Trabocchi, A.; Bessi, V.; Bagnoli, S.; Nacmias, B.; Credi, C.; Pavone, F. S. Multilayered Bioorthogonal SERS Nanoprobes Selectively Aggregating in Human Fluids: A Smart Optical Assay for β-Amyloid Peptide Quantification. *ACS Sens.* 2023, 8 (10), 3693−3700.

(31) Gupta, M. K.; Meng, F.; Johnson, B. N.; Kong, Y. L.; Tian, L.; Yeh, Y.-W.; Masters, N.; Singamaneni, S.; McAlpine, M. C. 3D Printed Programmable Release Capsules. *Nano Lett.* 2015, 15 (8), 5321−5329.

(32) García-Astrain, C.; Lenzi, E.; Jimenez de Aberasturi, D.; Henriksen-Lacey, M.; Binelli, M. R.; Liz-Marzán, L. M. 3D-Printed Biocompatible Scaffolds with Built-In Nanoplasmonic Sensors. *Adv. Funct. Mater.* 2020, 30 (45), 2005407.

(33) Zhu, K.; Shin, S. R.; van Kempen, T.; Li, Y.-C.; Ponraj, V.; Nasajpour, A.; Mandla, S.; Hu, N.; Liu, X.; Leijten, J.; et al. Gold Nanocomposite Bioink for Printing 3D Cardiac Constructs. *Adv. Funct. Mater.* 2017, 27 (12), 1605352.

(34) Miranda, B.; Moretta, R.; De Martino, S.; Dardano, P.; Rea, I.; Forestiere, C.; De Stefano, L. A PEGDA Hydrogel Nanocomposite to Improve Gold Nanoparticles Stability for Novel Plasmonic Sensing Platforms. *J. Appl. Phys.* 2021, 129 (3), 33101.

(35) Credi, C.; Bibikova, O.; Dallari, C.; Tiribilli, B.; Ratto, F.; Centi, S.; Pini, R.; Artyushenko, V.; Cicchi, R.; Pavone, F. S. Fiber-Cap Biosensors for SERS Analysis of Liquid Samples. *J. Mater. Chem. B* 2020, 8 (8), 1629−1639.

(36) Dallari, C.; Capitini, C.; Calamai, M.; Trabocchi, A.; Pavone, F. S.; Credi, C. Gold Nanostars Bioconjugation for Selective Targeting and SERS Detection of Biofluids. *Nanomaterials* 2021, 11, 665.

(37) Zhu, S.; Wang, X.; Cong, Y.; Liu, L.; Li, L. Free Radical Polymerization of Gold Nanoclusters and Hydrogels for Cell Capture and Light-Controlled Release. *ACS Appl. Mater. Interfaces* 2021, 13 (16), 19360−19368.

(38) Tomeckova, V.; Halloran, J. W. Critical Energy for Photopolymerization of Ceramic Suspensions in Acrylate Monomers. *J. Eur. Ceram. Soc.* 2010, 30 (16), 3273−3282.

(39) Jacobs, P. F. *Rapid Prototyping & Manufacturing: Fundamentals of Stereolithography*; Society of Manufacturing Engineers, 1992.

(40) Choi, J.; Wicker, R. B.; Cho, S.; Ha, C.; Lee, S. Cure Depth Control for Complex 3D Microstructure Fabrication in Dynamic Mask Projection Microstereolithography. *Rapid Prototyp. J.* 2009, 15 (1), 59−70.

(41) Yuan, H.; Khoury, C. G.; Hwang, H.; Wilson, C. M.; Grant, G. A.; Vo-Dinh, T. Gold Nanostars: Surfactant-Free Synthesis, 3D Modelling, and Two-Photon Photoluminescence Imaging. *Nanotechnology* 2012, 23 (7), 75102.

(42) Liu, X.; Atwater, M.; Wang, J.; Huo, Q. Extinction Coefficient of Gold Nanoparticles with Different Sizes and Different Capping Ligands. *Colloids Surf B Biointerfaces* 2007, 58 (1), 3−7.

(43) de Puig, H.; Tam, J. O.; Yen, C.-W.; Gehrke, L.; Hamad-Schifferli, K. Extinction Coefficient of Gold Nanostars. *J. Phys. Chem. C* 2015, 119 (30), 17408−17415.

(44) Gibson, I.; Rosen, D. W.; Stucker, B. *Additive Manufacturing Technologies*; Springer, 2010.

(45) Štaffová, M.; Ondreáš, F.; Svatík, J.; Zbončák, M.; Jančář, J.; Lepcio, P. 3D Printing and Post-Curing Optimization of Photopolymerized Structures: Basic Concepts and Effective Tools for Improved Thermomechanical Properties. *Polym. Test.* 2022, 108, 107499.

(46) Anseth, K. S.; Bowman, C. N.; Brannon-Peppas, L. Mechanical Properties of Hydrogels and Their Experimental Determination. *Biomaterials* 1996, 17 (17), 1647−1657.

(47) Credi, C.; Biella, S.; De Marco, C.; Levi, M.; Suriano, R.; Turri, S. Fine Tuning and Measurement of Mechanical Properties of Crosslinked Hyaluronic Acid Hydrogels as Biomimetic Scaffold Coating in Regenerative Medicine. *J. Mech. Behav. Biomed. Mater.* 2014, 29, 309−316.

(48) Cavallo, A.; Madaghiele, M.; Masullo, U.; Lionetto, M. G.; Sannino, A. Photo-Crosslinked Poly(Ethylene Glycol) Diacrylate (PEGDA) Hydrogels from Low Molecular Weight Prepolymer: Swelling and Permeation Studies. *J. Appl. Polym. Sci.* 2017, 134 (2), 44380.

(49) Mellott, M. B.; Searcy, K.; Pishko, M. V. Release of Protein from Highly Cross-Linked Hydrogels of Poly(Ethylene Glycol) Diacrylate Fabricated by UV Polymerization. *Biomaterials* 2001, 22 (9), 929−941.

(50) Innocenti, R.; Dallari, C.; Lenci, E.; Pavone, F. S.; Bianchini, F.; Credi, C.; Trabocchi, A. Design, Synthesis and Evaluation of RGD Peptidomimetic - Gold Nanostar Conjugates as M21 Cell Adhesion Inhibitors. *Bioorg. Chem.* 2022, 126, 105873.

(51) Kobayashi, K.; Ikuta, K. Three-Dimensional Magnetic Microstructures Fabricated by Microstereolithography. *Appl. Phys. Lett.* 2008, 92 (26), 262505.

(52) Wu, X.; Lian, Q.; Li, D.; Jin, Z. Tilting Separation Analysis of Bottom-up Mask Projection Stereolithography Based on Cohesive Zone Model. *J. Mater. Process. Technol.* 2017, 243, 184−196.

(53) Costa, B. N. L.; Adão, R. M. R.; Maibohm, C.; Accardo, A.; Cardoso, V. F.; Nieder, J. B. Cellular Interaction of Bone Marrow Mesenchymal Stem Cells with Polymer and Hydrogel 3D Microscaffold Templates. *ACS Appl. Mater. Interfaces* 2022, 14 (11), 13013−13024.

(54) Burke, G.; Devine, D. M.; Major, I. Effect of Stereolithography 3D Printing on the Properties of PEGDMA Hydrogels. *Polymers* 2020, 12, 2015.

(55) Tosetto, B.; Gastaldi, M.; Renno, G.; Pirri, C. F.; Barolo, C.; Fin, A.; Roppolo, I. Colorimetric 3D Printable Base-Detectors Exploiting Halocromic Core-Substituted Naphthalenediimides. *Polym. Chem.* **2023**, *14* (11), 1213−1223.

(56) Wang, L.; Liu, F.; Qian, J.; Wu, Z.; Xiao, R. Multi-Responsive PNIPAM-PEGDA Hydrogel Composite. *Soft Matter* **2021**, *17* (46), 10421−10427.

(57) Martínez-Ramos, I.; Maya-Mendoza, A.; Gariglio, P.; Aranda-Anzaldo, A. A Global but Stable Change in HeLa Cell Morphology Induces Reorganization of DNA Structural Loop Domains within the Cell Nucleus. *J. Cell. Biochem.* **2005**, *96* (1), 79−88.

(58) Chen, C.; Li, Z.; Xu, C.; Kang, M.; Lee, C.-S.; Aghaloo, T.; Lee, M. Self-Assembled Nanocomposite Hydrogels as Carriers for Demineralized Bone Matrix Particles and Enhanced Bone Repair. *Adv. Healthc. Mater.* **2024**, *13* (10), 2303592.